Ultrafast Photodoping and Plasmon Dynamics in FICO Nanocrystals for All-Optical Signal Manipulation at Optical Communication Wavelengths

Ilka Kriegel[a*], Carmine Urso[a,b], Daniele Viola[c], Luca De Trizio[a],Francesco Scotognella[a,d], Giulio Cerullo[c*] and Liberato Manna[a*]

[a] Italian Institute of Technology, Nanochemistry Department, via Morego 30, Genova, Italy

[b] University of Genoa, Department of Chemistry and Industrial Chemistry, via Dodecaneso 31, Genova, Italy

[c] IFN-CNR, Dipartimento di Fisica, Politecnico di Milano, P.za Leonardo da Vinci 32, Milano, Italy

[d] Center for Nano Science and Technology@PoliMi, Istituto Italiano di Tecnologia, Via Giovanni Pascoli 70/3, 20133 Milano, Italy

KEYWORDS doped metal oxide, plasmonic nanocrystals, ultrafast plasmon dynamics, photodoping, telecommunication wavelengths.

ABSTRACT: We show the ultrafast photodoping and plasmon dynamics of the near infrared (NIR) localized surface plasmon resonance (LSPR) of fluorine-indium codoped Cadmium Oxide (FICO) nanocrystals (NCs). The combination of high temporal resolution and broad spectral coverage allowed us to model the transient absorption (TA) spectra in terms of the Drude model, verifying the increase in carrier density upon ultrafast photodoping. Our analysis also suggests that a change in carrier effective mass takes place upon LSPR excitation, as a result of the non-parabolic conduction band of the doped semiconductor with a consequently high signal response. Both findings are specific to this new type of plasmonic material. The combination of large transmission modulation with modest pump powers and ultrafast recombination times make our results interesting for all-optical signal processing at optical communication wavelengths. At the same time, our results also give insights into the physical mechanisms of ultrafast photodoping and LSPR tuning of degenerately doped semiconductor NCs.

INTRODUCTION

The photo-induced alteration of the plasmonic response of nanomaterials delivers a tool for all-optical signal processing, enabling the design of novel optically controllable nanophotonic devices.[1–3] The combination of ultrafast signal manipulation with large transmittance variation is desirable for applications in active plasmonics and optical switching.[1,3,4] Degenerately doped semiconductor nanocrystals (NCs) are promising materials for these applications, as their free carrier density is much lower than in metals, so that the localized surface plasmon resonances (LSPRs) are more sensitive to absolute changes in the carrier concentration.[5–10] This enhanced sensitivity to the carrier density makes doped semiconductors appealing as active optical components, which require reversible modulation of either the strength or the frequency of the plasmon resonance and ultrafast response time for high switching rates.[4,6,11–19]

Degenerately doped metal oxide NCs can sustain heavy doping, reaching carrier concentrations in the range of $\sim 10^{21}$ cm^{-3}, which are intermediate between semiconductors and metals, resulting in LSPRs in the near infrared (NIR).[5–10] By controlling the level of doping and choosing from a library of materials, the LSPR can be designed to cover the spectral range from the NIR to the mid-IR.[5–10,19–34] Characteristics of the doped semiconductor nanostructures such as the non-parabolicity of the conduction band,[4] the presence of the bandgap with the associated transparency window in the visible range exploited for photodoping,[1,8–10,18,35–38] and the presence, in some cases, of crystalline anisotropy[25] offer new tools for signal manipulation. This, combined with ultrafast recovery times and large signal response, can make such systems interesting candidates for the development of ultrafast nanodevices.[1,2,4,18] Of high interest is in particular the option of all-optical switching, for example via the ultrafast photoexcitation of the LSPR.[2,4,6,12–19] Signal manipulation with photon energy greater than the bandgap, exciting valence band electrons into the conduction band and in turn altering the dielectric properties of the material, is another attractive option.[2,10,10,35,36,38] Due to the small volume of the NC, such photodoping can induce a switching from purely dielectric to metallic response.[2]

Most common doped metal oxides are based on a combination of aliovalent doping and oxygen vacancies.[9,39] Cation–anion codoping is an option to extend the spectral tunability of LSPRs in doped metal-oxides. Fluorine-Indium codoping of Cadmium Oxide (FICO) is as an at-

tractive example.[20,40] In this way LSPRs across a wavelength range from 1.5 to 3.3 μm are covered. Additionally, high quality factors of the plasmon resonance with narrow line widths are reached due to low impurity scattering.[20]

In this work, we demonstrate ultrafast all-optical manipulation of the LSPR in the NIR range at wavelengths relevant for optical communications. The all-optical photomodulation of the LSPR is achieved by exploiting the semiconducting and plasmonic properties of FICO NCs and by inducing two different physical scenarios: interband excitation, i.e. at 400 nm and LSPR excitation, i.e. at 1350 nm, while probing the LSPR between 1100 nm and 1650 nm. The combination of high temporal resolution and broad spectral coverage allowed us to model the transient absorption (TA) spectra and to extract the temporal evolution of the physical Drude parameters. This enabled us to explain the physical mechanisms underlying ultrafast signal modulation. While an increase in the carrier density due to ultrafast photodoping following interband pumping leads to a mono-exponential decay of the signal response due to electron-hole recombination, a change in carrier effective mass as a result of the non-parabolic conduction band might be the main reason for the large transient signal following LSPR pumping. The all-optical signal manipulation at telecommunication wavelengths combined with large transmission modulation at modest pump powers and ultrafast recombination times make our results interesting for ultrafast all-optical signal processing, and give insights into the physical properties of photodoping and LSPR tuning of degenerately doped semiconductor NCs.

EXPERIMENTAL SECTION

Chemicals. Oleic acid (90%), 1-octadecene (90%) and cadmium(II) acetylacetonate ($Cd(acac)_2$, >99.9%) were purchased from Sigma-Aldrich. Indium(III) fluoride (InF_3, 99.95%) was purchased from Alfa Aesar. Ethanol, toluene and chloroform were purchased from Carlo Erba. All chemicals were used without further purification.

Synthesis of FICO nanocrystals. 1.2mmol of $Cd(acac)_2$ was mixed of the desired amount of InF_3 in 1.67mL of oleic acid (5.25mmol) and 50mL of 1-octadecene. The solution was degassed under vacuum at 130°C for 1h, then it was put under nitrogen and the temperature was increased up to 315°C. This temperature was maintained for 45min. The produced NCs were washed three times by dispersion in chloroform followed by precipitation by addition of ethanol. Eventually the FICO NCs were dispersed in toluene and an additional cleaning step was performed by centrifugation at 1500rpm for 3min to get rid of bulky secondary products

Transmission electron microscopy (TEM) measurements. For the sample preparation dilute solutions of the NCs were dropped onto carbon coated copper grids. Low-resolution TEM measurements were carried out on a JEOL-1100 transmission electron microscope operating at an acceleration voltage of 100 kV.

X-ray diffraction (XRD) measurements. XRD measurements were performed on a Rigaku SmartLab X-ray diffractometer operating at 40 kV and 150 mA. The diffractometer was equipped with a Cu source and a Gobel mirror in order to have a parallel beam and it was used in 2-theta/omega scan geometry for the acquisition of the data. Specimens for the XRD measurements were prepared by dropping a concentrated NCs solution onto a zero-background silicon substrate.

Elemental Analysis. This was carried out via Inductively Coupled Plasma Optical Emission Spectroscopy (ICP-OES), using a iCAP 6500 Thermo spectrometer. All chemical analyses performed by ICP-OES were affected by a systematic error of about 5%. Samples were dissolved in HCl/HNO_3 3:1 (v/v).

UV-Vis-NIR absorption Spectroscopy. The UV-Vis-NIR absorption spectra of the NCs solutions in toluene were recorded using a Varian Cary 5000 UV-Vis-NIR absorption spectrophotometer.

Femtosecond TA spectroscopy. The ultrafast TA experiments were performed with a pump-probe setup based on a commercial Ti:sapphire amplified laser system delivering 100-fs pulses at 1 kHz repetition rate at a central wavelength of 800 nm. A fraction of the beam was either frequency doubled in a β-Barium Borate crystal to obtain 400 nm pump pulses, or used to drive a non-collinear parametric amplifier (NOPA) to generate pump pulses in the near-infrared between 1100 nm and 1400 nm, just off the plasmonic resonance of the sample (~1600 nm). The probe pulses were produced by focusing the fundamental beam into a 4 mm thick YAG plate in order to generate a stable white light supercontinuum reaching to 1650 nm. A long pass filter with cut-on wavelength at 950 nm was used to filter out the residual fundamental and the visible components of the probe pulse. The pump and probe beams were focused onto the sample with a spot size of around 300 μm. The pump-probe setup employed a computer-controlled optical multichannel analyzer (OMA) and the measured signal is a map of the chirp-free differential transmission $\Delta T/T = (T_{on}-T_{off})/T_{off}$ as a function of the pump-probe time delay for different probe wavelengths; T_{on} and T_{off} are the probe spectra transmitted by the excited and unperturbed samples, respectively. The OMA employed an InGaAs spectrometer (Bayspec SuperGamut NIR) that is able to detect from 870 nm to 1650 nm. All measurements were performed at room temperature on samples dissolved in toluene prepared under nitrogen atmosphere in a 1-mm-thick cuvette.

RESULTS AND DISCUSSION

FICO NCs were synthesized by following a procedure published elsewhere[20] (see the Experimental Section for details). Two different FICO samples were prepared by varying the molar ratio of InF_3, employed as both indium and fluorine dopants precursor, from 20% to 30% with respect to $Cd(acac)_2$. In Figure 1 we show the absorption spectrum of two typical samples of FICO NCs with LSPRs in the NIR peaking at 1625 nm and 1550 nm, respectively. The resulting NCs had a spherical shape (see inset in Figure 1a) with diameters around 10 nm and their crystal structure was as-

signed to bulk CdO, as evidenced by our XRD measurements (see Figure 1a-b). The molar concentration of In dopant, as determined by ICP elemental analysis and calculated as In/(In+Cd), was 7.5 % for the longer wavelength LSPR sample and 15.5% for the shorter wavelength LSPR one. The blue-shift of the plasmon resonance is in agreement with the measured higher level of doping that leads to an increased carrier density.

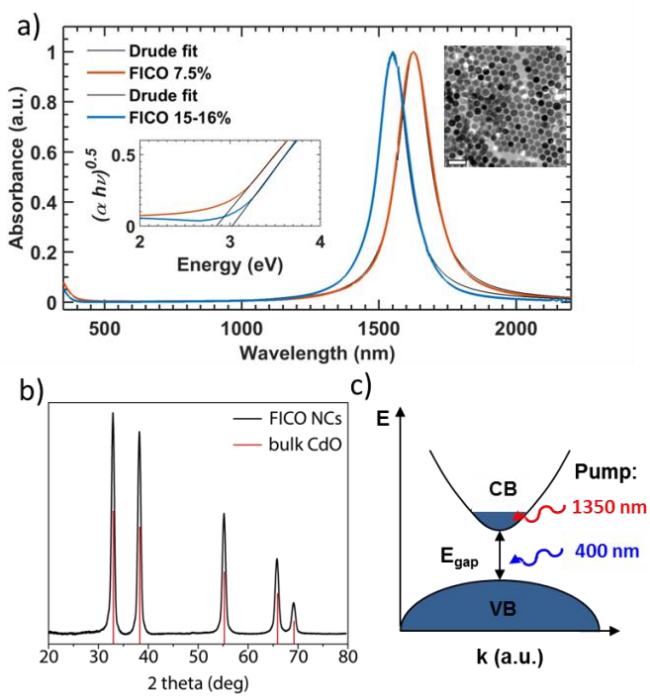

Figure 1. (a) Steady state absorption spectra of two typical FICO NC samples with different doping levels with their LSPR peaking at 1550 nm (blue – 15.5% In) and 1625 nm (red – 7.5% In), together with a typical TEM micrograph (the scale bar is 50 nm). The thin black curves represent their spectral fits with the Drude model and the Mie theory in the quasi-static approximation. (inset) The inset shows the $(\alpha h\nu)^2$-hν plots, for the two FICO samples. The value of the optical band gap (E_{gOPT}) can be derived from the extrapolation to α=0. (b) XRD pattern of the FICO NCs, with crystal structure matching that of bulk CdO (ICSD number 24802). (c) Illustration of the band diagram of the doped NC, where shaded blue areas depict occupied states in the valence and the conduction band (VB and CB, respectively), separated by the energy gap E_{gap}. In this work we performed two sets of experiments, by pumping either the interband transition, i.e. with 400 nm pulses, or the intraband region, i.e. with 1350 nm pulses, as depicted by blue and red arrows, respectively.

The steady state absorption spectra of the FICO NCs in the NIR region were quantitatively modeled using the quasi-static approximation of the Mie theory, according to which the absorption cross section σ_A can be expressed as:

$$\sigma_A(\omega) = \frac{4\pi\omega}{c}\sqrt{\varepsilon_H}\cdot R^3 \cdot imag\left(\frac{\varepsilon_{p(\omega)}-\varepsilon_H}{\varepsilon_{p(\omega)}+2\cdot\varepsilon_H}\right) (1)$$

where ε_H is the frequency independent dielectric constant of the environment (the solvent for measurements in solution), $\varepsilon_p(\omega)$ the frequency dependent dielectric function of the material, R the nanoparticle radius, c the wavelength of light, and ω the frequency. The absorption of the NC solution was then calculated according to the Lambert-Beer law as:

$$A = \frac{N\cdot\sigma_A\cdot L}{\log(10)}, N = \frac{3v_F}{4\pi R^3} (2)$$

where N is the number density of NCs in solution, L represents the path length of the cuvette and v_F is the fill factor. The dielectric function $\varepsilon_p(\omega)$ of the free carriers in the FICO NCs in the NIR is described by the Drude model:

$$\varepsilon_p(\omega) = \varepsilon_\infty - \frac{\omega_p^2}{(\omega^2+i\omega\Gamma)} (3)$$

where the parameter ε_∞ depicts the high frequency dielectric constant, and Γ is the free carrier damping constant. The plasma frequency ω_p of the free carriers is given by

$$\omega_p = \sqrt{\frac{ne^2}{\varepsilon_0 m^*}} (4)$$

with e being the electron charge, m^* the effective mass, ε_o the vacuum dielectric permittivity, and n the carrier density. As seen in Figure 1a (black thin curves), excellent fit results were obtained. The extracted value of Γ=540 cm^{-1} (0.07 eV) illustrates the very narrow linewidths of the NC LSPRs. The LSPR quality factor for these FICO NCs, defined as the ratio between the peak energy position $E(eV)$ and the width $\Delta E(eV)$ of the LSPR, is in the range of 10. Similar quality factors have been published by Ye *et al.*[20] for the same material, and are among the highest for the class of heavily doped semiconductor NCs. We calculated a value of ε_∞=5.6 that is in agreement with what is reported for Cadmium Oxide bulk materials.[41,42] The plasma frequency ω_p, that depends on the level of doping, was calculated to be between 18700 and 19700 cm^{-1} (2.32-2.44 eV). Eventually, using m^* = 0.43m_o as the effective mass of the carriers, the carrier density could be estimated to be around 1.68 - $1.86\cdot10^{+21}$ cm^{-3}.[42]

In the UV-vis region of the spectra the onset of the interband absorption of FICO NCs was observed to blue-shift with increasing the amount of In doping (see Figure 1a). The blue-shift of the optical bandgap, better illustrated by the Tauc plots in the inset of Figure 1a, is a result of the well-known Moss-Burstein effect of heavily doped semiconductors and confirms, once again, the effective increase in free carriers concentration when going from 7.5% to 15.5% of In doping.[7,10,20,21,43] Notable is the transparency region between the interband absorption onset and the LSPR peak. The fact that the bandgap is well separated from the LSPR allowed us to perform experiments where the interband and the intraband regime could be excited separately, while probing in the region of the LSPR. Thus, we had two distinct ways to induce an ultrafast modification of the LSPR in the NIR. Figure 1c sketches the band diagram of the FICO NCs separated by the energy gap E_g, where shaded areas depict filled states in the valence band (VB) and in the conduction band (CB). For the bandgap excitation, we chose to pump at 400 nm, which is just above the bandgap, in order to avoid the creation of carriers with excess energy and thus sample heating (blue arrow in Figure 1c). For the excitation of the LSPR we selected a pump wavelength just

off the LSPR maximum at around 1350 nm (red arrow in Figure 1c). For the following experiments we chose a sample with the maximum LSPR at 1610 nm.

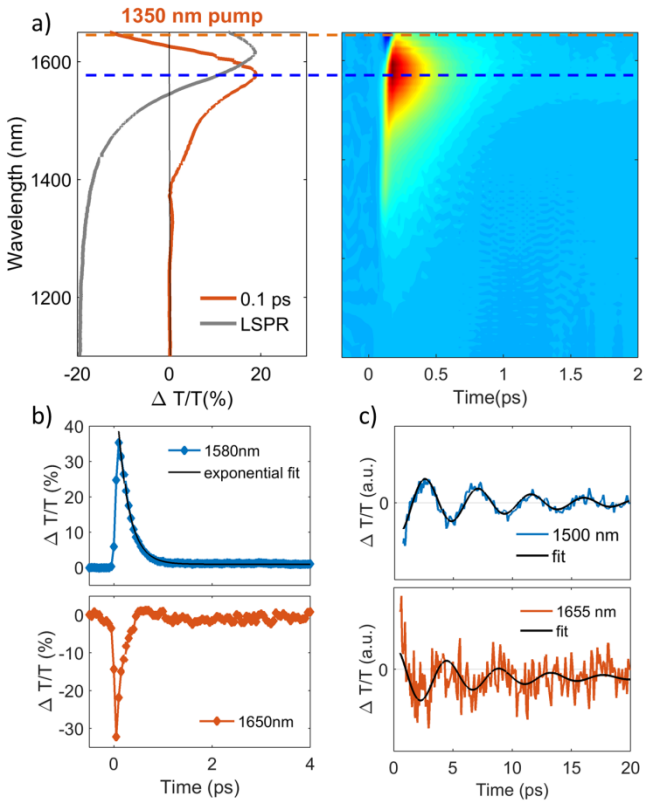

Figure 2. Transient optical response of FICO following intraband excitation. a) Representative TA spectrum at the maximum rise time around 100 fs after photoexcitation, exhibiting a derivative shaped curve (left) together with the two-dimensional Δ T/T map (right), showing the signal as a function of pump–probe delay and probe wavelength for FICO NCs excited at 1350 nm with an excitation density 0.13 mJ/cm^2. The steady state LSPR absorption spectrum is also given in grey for comparison. (b) Transient decay dynamics at 1580 nm together with a bi-exponential fit (black and blue curve, respectively, upper panel) and 1650 nm (red curve lower panel), illustrated by the horizontal cuts (dashed lines) depicted in panel (a). (c) Δ T/T time traces extracted at the selected probe wavelengths to the red (around 1600 nm) and the blue (1500 nm) of the maximum PB signal after subtracting the bi-exponential decay, along with their fits by a damped sinusoidal function (black curves). The extracted oscillating period is T = 4.4 ps and the damping time constant is τ= 7 ps.

Figure 2 depicts the results of the TA experiments following intraband LSPR excitation with 1350 nm pump pulses. The transient spectrum at around 0.1 ps delay time (corresponding to the maximum of the TA signal) is presented together with the two-dimensional ΔT/T map showing the signal as a function of the pump–probe delay and the probe wavelength. In grey is given the steady state spectrum around the LSPR for comparison. The signal can be described by a derivative shape with a photobleaching (PB) maximum to the blue of the LSPR and a photoinduced absorption (PA) to the red. As a reminder, a positive ΔT/T signal corresponds to an increased transmission, which indeed is a result of the bleaching of the signal, hence PB. The decay dynamics of the TA signal is shown in Figure 2b for the PB maximum at 1580 nm together with a bi-exponential fit with the time constants of 0.23 and 38 ps, respectively (black curve). The maximum PA signal at 1650 nm instead is decaying within less than 1 ps (red curve, lower panel). Indeed, the non-linear optical response of plasmonic resonances follows a specific trend corresponding to two well-separated temporal dynamics: a short-time dynamics in the picosecond time range and a longer decay dynamics of several tens to hundreds of picoseconds.[4,6,14,15,44] The excitation of the free carriers with an intense laser pulse (pump pulse) in the region of the LSPR results in the creation of a non-thermal distribution of the Fermi gas. Strong carrier-carrier scattering leads to the establishment of a new Fermi distribution with a higher carrier temperature, observed as the maximum non-linearity of the transient signal. Subsequently the carriers cool down via the emission of phonons to the NCs lattice (initial fast decay) and by the following release of energy to the surrounding via phonon-phonon coupling (second slower decay).[44,45] The change in carrier and lattice temperatures after excitation causes a temporal modification of the dielectric function of the material, probed at controlled time delays after excitation.[46,47] The non-linearities observed by us in the region of the LSPR have a very similar modulation, showing an initial fast decay within 1 ps, ascribed to the initial phonon emission (carrier–phonon), and the subsequent slower decay, ascribed to phonon–phonon scattering and heat dissipation into the solvent.[4,6,11–19] Generally the initial fast decay dynamics is rather fast with respect to noble metals, which display time constants of the order of 1 ps for electron phonon coupling. This is explained by the lower heat capacity of the carriers in the doped semiconductor and the lower carrier density with respect to noble metals, as also shown for indium tin oxide (ITO) nanopillars[4] and $Cu_{2-x}S$ NCs.[13,15] We observe a linear increase in the ΔT/T signal with pump power (see Supporting Information Figure S2), reaching 80% for an excitation density of 0.3 mJ/cm^2 only. Power dependent measurements reveal a slight increase in the fast initial decay time, due to the higher density of photoexcited carriers. A careful comparison of the spectra reveals a slight blue shift of the TA spectra with increasing the pump power (see Supporting Information Figure S3). We will refer to this point later.

Notably, the ultrafast increase in the lattice temperature due to carrier–phonon coupling leads to a change in the equilibrium volume of the NC and the impulsive excitation of coherent vibrational (breathing) modes.[48,49] As a result of the heat induced NC volume change the surface plasmon resonance condition is affected, leading to a temporal shift of the LSPR, which is observed as oscillations to the red and to the blue of the maximum bleach non-linearity overlaying the second slower decay. Indeed, we observed such oscillations at around 1500 nm and at 1655 nm, as shown in Figure 2c. By fitting the period of the oscillations with a damped sine function and by previously subtracting

the slowly varying second exponential decay, the period T and the damping τ of the oscillation can be extracted:[48,50,51]

$$F(t) = A \cdot e^{-t/\tau} \cdot \sin\left(\frac{2\pi t}{T} + \phi\right) \quad (5)$$

where A is the initial amplitude, and ϕ is the initial phase. The oscillations after subtracting the underlying two-step decay dynamics together with the fit results are plotted as in Figure 2c. It is worth noting that a π phase shift occurs for wavelengths at different sides of the LSPR, as expected from oscillations arising from a periodic shift of an optical resonance. Taken together, these results follow the typical transient dynamics of plasmonic materials.

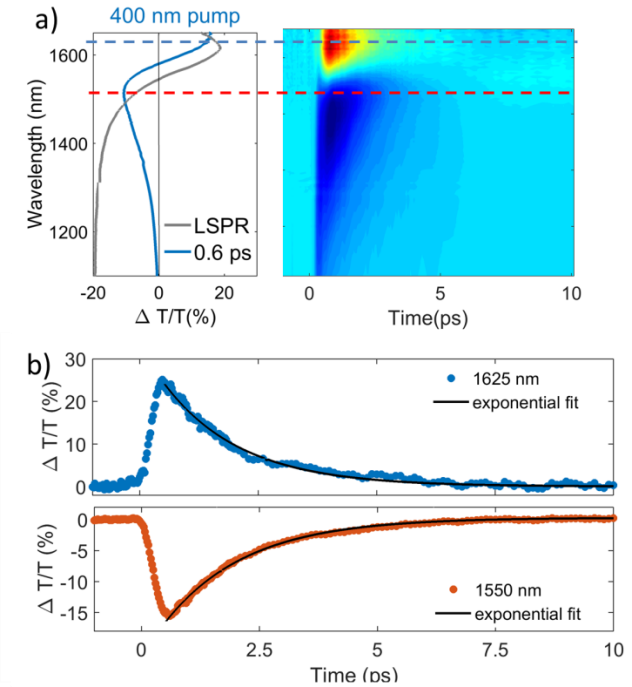

Figure 3. Transient optical response of FICO following interband excitation. (a) TA spectrum at the maximum signal (0.6 ps) showing the typical derivative shaped curve together with the two-dimensional ΔT/T map showing the signal as a function of pump–probe delay and probe wavelength for FICO NCs excited at 400 nm for the excitation density 2.35 mJ/cm^2. The steady state LSPR absorption spectrum is also given in grey for comparison. (b) Transient decay dynamics at 1625 nm (blue curve upper panel) and 1550 nm (red curve lower panel) together with the mono-exponential fits (black curve), illustrated by the horizontal cuts (dashed lines) depicted in panel (a).

The TA results following intergap excitation at 400 nm are given in Figure 3. Figure 3a depicts a TA spectrum at the maximum of the signal rise time at 0.6 ps, corresponding to the peak to the signal build-up, together with the two-dimensional ΔT/T map showing the signal as a function of the pump–probe delay and the probe wavelength. The spectrum is described by a derivative shaped signal modulation with negative signal, i.e. a PA at wavelengths to the blue of the maximum of the steady state LSPR spectrum and a PB signal to the red, displaying the opposite modulation as observed for the intraband LSPR pumping. We will come back to this point later. For comparison we give in grey the steady state spectrum around the LSPR. Figure 3b displays the decay dynamics for the PA maximum at 1550 nm (blue curve) and the PB maximum at 1625 nm (red curve), illustrated by the horizontal cut (dashed line) in panel (a). The decay can be fit by a mono-exponential curve with a time constant of 1.7 ps (black curves in Figure 3b), showing a fundamentally different recovery mechanism occurring here in comparison to what is observed in the LSPR pumping. Note that the time axis in the two-dimensional ΔT/T map of Figure 2a for the LSPR excitation is only 2 ps compared to the 10 ps here, evidencing the much faster signal modulation when pumping the LSPR versus the interband transition. A short rise time of the signal in the range of 600 fs is observed followed by a mono-exponential decay. Pump power dependent measurements reveal no changes in the decay dynamics (see Supporting Information Figure S4 for details) and a linear increase of the signal intensity. Interband pumping at 400 nm excites electrons from the valence band to the conduction band. This increases the carrier density by capacitive charging and in turn results in the modification of the LSPR. We propose that the mono-exponential decay is a result of the temporarily increased carrier density n after the ultrafast photodoping that decays with the electron-hole recombination time. Pump-power dependent measurements display an additional red-shift of the derivative shaped signal with increasing the pump power in correspondence with a further increased carrier density (see Figure S5 in the Supporting Information). These findings, thus, are the first demonstration of ultrafast photodoping of degenerately doped semiconductor NCs, and a way to control the LSPR specific to degenerately doped semiconductors.[7–10,35,36]

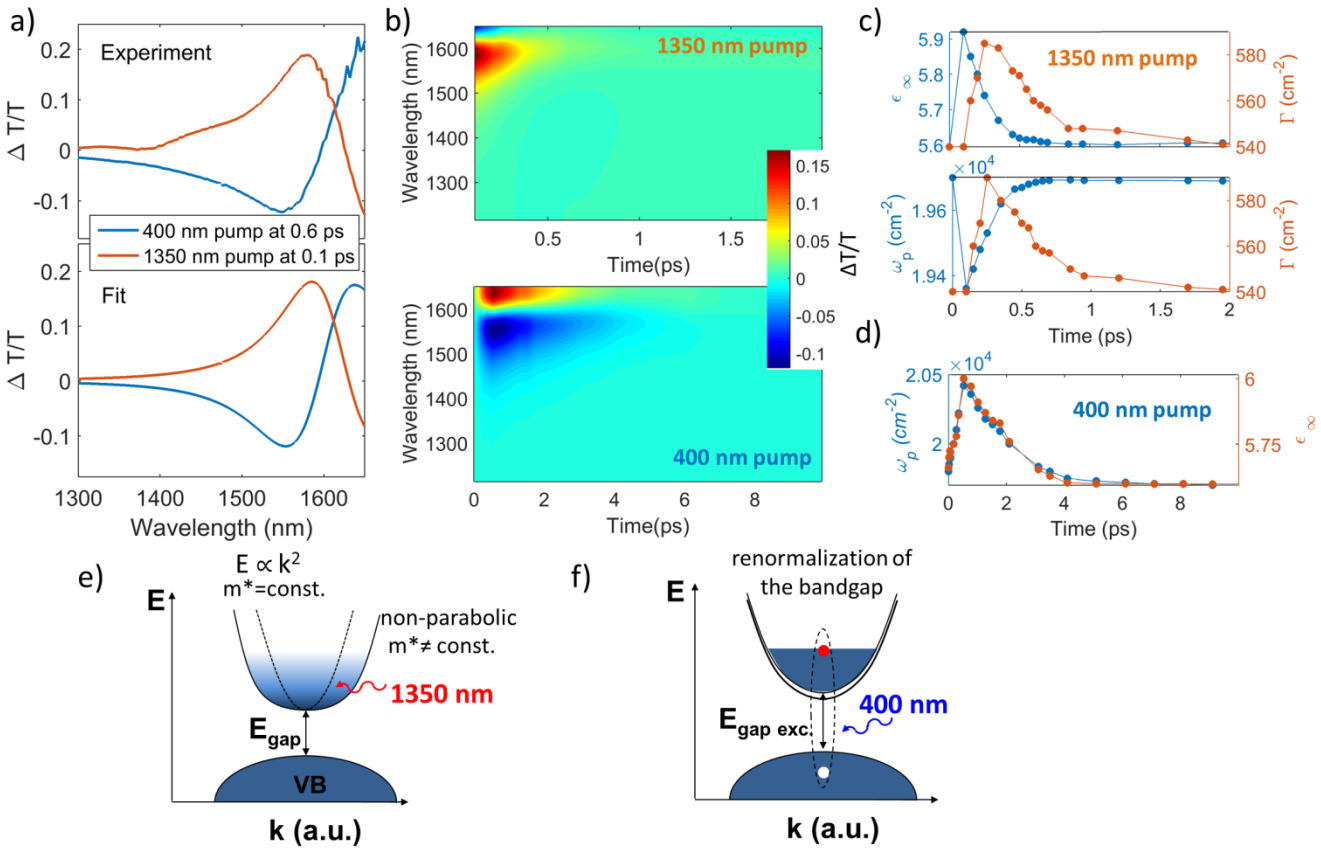

Figure 4. (a) Upper panel: Comparison of the experimental results of the two different pump scenarios: bandgap pumping (400 nm pump - interband, blue curve) and LSPR pumping (1350 nm pump - intraband, red curve). The pump induced modification of the transient spectra at the early times displays the reverse modulation of the spectra, indicating a fundamentally different origin of the TA signal. Lower panel: the corresponding fits according to the model described in the text. (b) Fit results plotted as a two-dimensional ΔT/T map showing the signal as a function of pump–probe delay and probe wavelength for the excitation with 1350 nm (upper panel) and the excitation with 400 nm (lower panel). c) Fit parameters of the LSPR pumping (1350 nm pump - , intraband) plotted versus time. Upper panel: fit with varying dielectric constant ε_∞ and damping parameter Γ; lower panel: fit with varying plasma frequency ω_p and damping parameter Γ. d) Fit parameters of the bandgap pumping (400 nm pump - , interband) plotted versus time. e) Sketch of the non-parabolic (solid lines) versus the parabolic band $E \propto k^2$ (dashed line) after 1350 nm excitation. The non-parabolic band structure has the effect that the effective mass increases for higher energy states instead of being constant in a parabolic band. f) Illustration of the bandgap renormalization due to the presence of an electron in the valence band and an electron in the conduction band after 400 nm excitation, which in turn influences the absorption properties in the high frequency range, i.e. ε_∞.

To shed light on the exact mechanisms of LSPR modification we performed optical modeling of the TA spectra. The transient signal is triggered by the pump induced modulation of the FICO NCs' dielectric function. For this we take into account the modified Drude dielectric function $\varepsilon_p(\omega,t)$, which is varying with time t:

$$\varepsilon_p(\omega,t) = \varepsilon_\infty(t) + \frac{\omega_p(t)}{\omega^2+\Gamma^2(t)} + i\frac{\omega_p(t)\Gamma(t)}{\omega(\omega^2+\Gamma^2(t))} \quad (6)$$

The TA results are then modeled by taking into account the sample transmission

$$T(\omega) = \exp\frac{-\sigma_A(\omega)\cdot N\cdot L}{log(10)} \quad (7)$$

retrieved from the steady state absorption spectrum (Equations 1-4). The transient variation of the absorption cross section $\Delta\sigma_A(\omega,t)$, due to the variation of the material dielectric constant $\varepsilon_p(\omega,t)$, then allows to calculate the transient transmission of the sample by

$$\frac{\Delta T}{T}(\omega) = \exp\frac{-\Delta\sigma_A(\omega,t)\cdot N\cdot L}{\log(10)} - 1 \quad (8)$$

In the upper panel of Figure 4a the experimental results of the two different pump scenarios are compared at early times. Both TA show a derivative shape while the reverse modulation is observed for the 400 nm pump (blue curve) with respect to the 1350 nm pump (red curve), indicating a fundamentally different origin of the pump-induced signal variation. The fits of the spectra (400 nm pump, blue curve and 1350 nm pump, red curve in Figure 4a, lower panel)

show an excellent agreement with the experimental results. By fitting the transient optical response of FICO NCs with time we were able to plot the two-dimensional ΔT/T map as a function of the pump–probe delay and the probe wavelength for both pump wavelengths: (upper panel) intraband pumping at 1350 nm and (lower panel) interband pumping at 400 nm. For comparison we give the experimental maps of this set of data in the Supporting Information (Figure S6). The fit parameters of $\varepsilon_\infty(t)$, $\omega_p(t)$, and $\Gamma(t)$ are given in Figure 4c (1350 nm pump) and Figure 4d (400 nm pump). We first consider the case of the LSPR pumping at 1350 nm. We were able to accurately model the TA spectra by increasing the high frequency dielectric constant $\varepsilon_\infty(t)$ from its original value of 5.6 to 6.2 and the resulting time dependent $\varepsilon_\infty(t)$ is shown in the upper panel of Figure 4c (blue curve). An ultrafast recovery of the initial value within less than one picosecond is observed, thereafter a tail with a minor variation remains. Notably, the maximum modulation is reached within 100 fs. Thereafter it decays with a time constant of less than 0.2 ps. Together with the decay of the high frequency dielectric constant an increase of the damping term Γ is prompted reaching its maximum value at around 0.25 ps, before it decays rapidly, remaining quasi constant at slightly elevated values after around 2.5 ps. Our results fit well with the assumptions of the Drude-Sommerfeld model of the free electron, stating that the heating of the carriers, and subsequently, of the lattice induce a change in the dielectric function of a metallic material. Such picosecond variations, due to the cooling of the hot carriers, and the subsequent heat transfer to the lattice, are quantitatively accounted for by the two-temperature model.[46] The initial heating of the carrier gas leads to a non-thermal distribution of the carriers and a smearing of the Fermi distribution, which, in turn, results in the modulation of the interband transition, and thus of the high frequency dielectric constant $\varepsilon_\infty(t)$.[46] The heating of the lattice instead causes a modulation of the Γ parameter because of the increased electron–phonon scattering rate with temperature.[4] Thus, the initial fast decay, extracted for the variation of the high frequency dielectric constant ε_∞, can be ascribed to the cooling of the hot carriers that modifies the absorption in the high frequency range, and in turn induces the heating of the lattice observed as increased damping Γ.

It is notable that we were equally able to fit our transient spectra by varying the plasma frequency ω_p, whilst obtaining very similar values for the damping term Γ (see Figure 4c, lower panel). Indeed, in a recent work by Guo et al.[4] on ITO nano rod arrays, the authors relate the observed nonlinear optical response to a change of the plasma frequency of ITO, instead of the Fermi-surface smearing and the related change in ε_∞. As a variation of the carrier density n cannot be induced via intraband pumping, the observed pump-induced redshifts of the LSPRs have been ascribed to the change in the effective mass of the carriers m^*.[4] The latter is ascribed to the conduction band non-parabolicity, an effect observed in several highly-doped metal oxides.[4,42] The non-parabolic band structure has the effect that the effective mass increases for higher energy states as it becomes k-vector dependent, while in the parabolic band limit it would remain constant. This effect is illustrated in a sketch in Figure 4d. As a result of the lower carrier density with respect to noble metals, a remarkable change is induced to the electron distribution upon LSPR pumping and a significant plasma frequency modulation is observed. Also for indium doped cadmium oxide (ICO) a non-parabolic band has been determined,[42] which means that the variation of ω_p due to a change in the effective carrier mass after the excitation might be the physical origin of the transient response following the LSPR excitation. Indeed, we observe a more marked red shift at higher pumping power indicating that a higher fraction of free carriers are probing regions of higher momentum in the conduction band, hence have their effective mass increased. Similar findings have been made by Guo et al.[4] and support the picture of the non-parabolic band for FICO NCs.

Besides the effective mass m^*, a change in carrier density can also alter the plasma frequency ω_p. Indeed, by prompting interband transitions the carrier density in the conduction band of a metal oxide can be optically enhanced via photodoping.[10,18,38] As the free carrier density in doped semiconductors is much lower than in metals their LSPRs are more sensitive to absolute changes in the carrier concentration and LSPR blue-shifts are observed.[10,18,38] The direct photoexcitation of a doped semiconductor at energies near the bandgap increases the carrier density and thereby increases ω_p, resulting in a blue-shift of the LSPR. Thus, we assume that the 400 nm excitation, i.e. above the band edge of FICO NCs, manipulates their plasma frequency on the ultrafast time scale by the injection of electrons into, and their subsequent decay from, the conduction band. This is further supported by an additional blue shift of the signal with higher pump power (see Figure S 5 in the Supporting Information). Indeed, by fitting the TA spectra we find that the signal modulation is reproduced by increasing ω_p. The maximum modification $\Delta\omega_p$ would then result in an increase in carrier density by 7.5 % (see Equation (4) and by assuming a constant effective mass of $0.43m_o$). The temporal evolution of $\omega_p(t)$ with time shows a mono-exponential dynamics, which displays a similar temporal evolution as the decay of the maximum PB and the PA signal shown in Figure 3b. This indicates that, indeed, the change in ω_p is inducing the signal modulation and it confirms our picture of the transient increase of carrier density. Remarkably, we found that simultaneously with the $\omega_p(t)$ we had to adjust also the high frequency dielectric constant $\varepsilon_\infty(t)$. The variation shows the same behavior as $\omega_p(t)$ thus displaying a linear relationship between ε_∞ and ω_p. While in doped metal oxides ε_∞ has been shown to linearly decrease by increasing the doping level, in our case we observed the opposite trend. The former is understood in terms of the widening of the bandgap as a consequence of the Moss-Burstein effect, which leads to higher transparency at higher frequencies.[8,43] However, in our case we are considering a slightly different system in which the extra carrier added through photodoping is connected to the formation of a hole in the valence band. Coulomb interactions between electrons and holes, or band gap renormalization due to the occupation of states in the system, might

be responsible for the observed increase in ε_∞.[52] This effect is illustrated in Figure 4f showing a sketch of valence and conduction band and the electron and hole pair after photoexcitation with 400 nm pump pulses. Our finding illustrates a fundamental difference between chemical doping and capacitive charging via photodoping, and a deeper evaluation of this finding would involve the observation of the spectral and temporal evolution with the addition of a hole scavenger to the solution or upon surface modification of the NCs, which results in an influence of the electron-hole interaction.[35,36,53] We remark here that also the carrier damping was slightly adjusted during the spectral fits showing an initial rise and an immediate decay within the first hundreds of femtoseconds, which might be assigned to the cooling of carriers with excess energy and also explains the initial signal rise time.

Conclusion

Ultrafast all-optical signal modulation at telecommunication wavelengths was shown in FICO NCs, a material system possessing extremely narrow and high quality LSPRs that are tunable in the NIR. Bandgap (at 400 nm) and LSPR (at 1350 nm) pumping allowed us to induce ultrafast signal modulation of the LSPR, according to two fundamentally different excitation processes. LSPR pumping results in the typical two-step decay due to carrier and lattice heating and to the impulsive excitation of the radial breathing mode. In contrast, a mono-exponential decay of the signal was observed after bandgap pumping assigned to the ultrafast photodoping induced carrier density increase, confirmed by rigorous optical modeling. Photodoping is a means of LSPR control based on capacitive charging of the semiconductor, specific to doped metal oxides. Notably, the temporal evolution after the LSPR excitation at early times could be ascribed to the change of ε_∞, as known from noble metals and other plasmonic material.[13,15,44,47] However, we were equally able to reproduce the spectra by a decrease of the plasmon frequency ω_p, which is a result of the k-vector dependent effective mass in the non-parabolic band of indium doped cadmium oxide, a characteristic that is specific to metal oxides and delivers a new physical variable for LSPR modification.[4] Taken together the observed combination of ultrafast recovery times and large transmission change make FICO NCs interesting candidates for the development of all-optical modulators in novel nanodevices functioning at wavelength relevant for optical communication.

ASSOCIATED CONTENT

Supporting Information. Pump power dependent, experimental two-dimensional maps corresponding to the fit data. This material is available free of charge via the Internet at http://pubs.acs.org.

AUTHOR INFORMATION

Corresponding Author

*Corresponding author: ilka.kriegel@iit.it, giulio.cerullo@polimi.it, liberato.manna@iit.it

.

REFERENCES

(1) Kinsey, N.; DeVault, C.; Kim, J.; Ferrera, M.; Shalaev, V. M.; Boltasseva, A. Epsilon-near-Zero Al-Doped ZnO for Ultrafast Switching at Telecom Wavelengths. *Optica* **2015**, *2* (7), 616–622.

(2) Babicheva, V. E.; Boltasseva, A.; Lavrinenko, A. V. Transparent Conducting Oxides for Electro-Optical Plasmonic Modulators. *Nanophotonics* **2015**, *4* (1).

(3) Ni, G. X.; Wang, L.; Goldflam, M. D.; Wagner, M.; Fei, Z.; McLeod, A. S.; Liu, M. K.; Keilmann, F.; Özyilmaz, B.; Neto, A. H. C.; et al. Ultrafast Optical Switching of Infrared Plasmon Polaritons in High-Mobility Graphene. *Nat. Photonics* **2016**, *10* (4), 244–247.

(4) Guo, P.; Schaller, R. D.; Ketterson, J. B.; Chang, R. P. H. Ultrafast Switching of Tunable Infrared Plasmons in Indium Tin Oxide Nanorod Arrays with Large Absolute Amplitude. *Nat. Photonics* **2016**, *10* (4), 267–273.

(5) Dorfs, D.; Härtling, T.; Miszta, K.; Bigall, N. C.; Kim, M. R.; Genovese, A.; Falqui, A.; Povia, M.; Manna, L. Reversible Tunability of the Near-Infrared Valence Band Plasmon Resonance in Cu2–xSe Nanocrystals. *J. Am. Chem. Soc.* **2011**, *133* (29), 11175–11180.

(6) Kriegel, I.; Jiang, C.; Rodríguez-Fernández, J.; Schaller, R. D.; Talapin, D. V.; da Como, E.; Feldmann, J. Tuning the Excitonic and Plasmonic Properties of Copper Chalcogenide Nanocrystals. *J. Am. Chem. Soc.* **2012**, *134* (3), 1583–1590.

(7) Luther, J. M.; Jain, P. K.; Ewers, T.; Alivisatos, A. P. Localized Surface Plasmon Resonances Arising from Free Carriers in Doped Quantum Dots. *Nat. Mater.* **2011**, *10* (5), 361–366.

(8) Garcia, G.; Buonsanti, R.; Runnerstrom, E. L.; Mendelsberg, R. J.; Llordes, A.; Anders, A.; Richardson, T. J.; Milliron, D. J. Dynamically Modulating the Surface Plasmon Resonance of Doped Semiconductor Nanocrystals. *Nano Lett.* **2011**, *11* (10), 4415–4420.

(9) Lounis, S. D.; Runnerstrom, E. L.; Llordes, A.; Milliron, D. J. Defect Chemistry and Plasmon Physics of Colloidal Metal Oxide Nanocrystals. *J. Phys. Chem. Lett.* **2014**, *5* (9), 1564–1574.

(10) Schimpf, A. M.; Gunthardt, C. E.; Rinehart, J. D.; Mayer, J. M.; Gamelin, D. R. Controlling Carrier Densities in Photochemically Reduced Colloidal ZnO Nanocrystals: Size Dependence and Role of the Hole Quencher. *J. Am. Chem. Soc.* **2013**, *135* (44), 16569–16577.

(11) Ludwig, J.; An, L.; Pattengale, B.; Kong, Q.; Zhang, X.; Xi, P.; Huang, J. Ultrafast Hole Trapping and Relaxation Dynamics in P-Type CuS Nanodisks. *J. Phys. Chem. Lett.* **2015**, *6* (14), 2671–2675.

(12) Riha, S. C.; Schaller, R. D.; Gosztola, D. J.; Wiederrecht, G. P.; Martinson, A. B. F. Photoexcited Carrier Dynamics of Cu2S Thin Films. *J. Phys. Chem. Lett.* **2014**, *5* (22), 4055–4061.

(13) Scotognella, F.; Della Valle, G.; Srimath Kandada, A. R.; Dorfs, D.; Zavelani-Rossi, M.; Conforti, M.;

Miszta, K.; Comin, A.; Korobchevskaya, K.; Lanzani, G.; et al. Plasmon Dynamics in Colloidal Cu $_{2-x}$ Se Nanocrystals. *Nano Lett.* **2011**, *11* (11), 4711–4717.

(14) Scotognella, F.; Valle, G. D.; Kandada, A. R. S.; Zavelani-Rossi, M.; Longhi, S.; Lanzani, G.; Tassone, F. Plasmonics in Heavily-Doped Semiconductor Nanocrystals. *Eur. Phys. J. B* **2013**, *86* (4), 1–13.

(15) Della Valle, G.; Scotognella, F.; Kandada, A. R. S.; Zavelani-Rossi, M.; Li, H.; Conforti, M.; Longhi, S.; Manna, L.; Lanzani, G.; Tassone, F. Ultrafast Optical Mapping of Nonlinear Plasmon Dynamics in Cu2–xSe Nanoparticles. *J. Phys. Chem. Lett.* **2013**, *4* (19), 3337–3344.

(16) Xie, Y.; Carbone, L.; Nobile, C.; Grillo, V.; D'Agostino, S.; Della Sala, F.; Giannini, C.; Altamura, D.; Oelsner, C.; Kryschi, C.; et al. Metallic-like Stoichiometric Copper Sulfide Nanocrystals: Phase- and Shape-Selective Synthesis, Near-Infrared Surface Plasmon Resonance Properties, and Their Modeling. *ACS Nano* **2013**, *7* (8), 7352–7369.

(17) Alam, R.; Labine, M.; Karwacki, C. J.; Kamat, P. V. Modulation of Cu2–xS Nanocrystal Plasmon Resonance through Reversible Photoinduced Electron Transfer. *ACS Nano* **2016**, *10* (2), 2880–2886.

(18) Tice, D. B.; Li, S.-Q.; Tagliazucchi, M.; Buchholz, D. B.; Weiss, E. A.; Chang, R. P. H. Ultrafast Modulation of the Plasma Frequency of Vertically Aligned Indium Tin Oxide Rods. *Nano Lett.* **2014**, *14* (3), 1120–1126.

(19) De Trizio, L.; Gaspari, R.; Bertoni, G.; Kriegel, I.; Moretti, L.; Scotognella, F.; Maserati, L.; Zhang, Y.; Messina, G. C.; Prato, M.; et al. Cu3-xP Nanocrystals as a Material Platform for Near-Infrared Plasmonics and Cation Exchange Reactions. *Chem. Mater.* **2015**, *27* (3), 1120–1128.

(20) Ye, X.; Fei, J.; Diroll, B. T.; Paik, T.; Murray, C. B. Expanding the Spectral Tunability of Plasmonic Resonances in Doped Metal-Oxide Nanocrystals through Cooperative Cation–Anion Codoping. *J. Am. Chem. Soc.* **2014**, *136* (33), 11680–11686.

(21) Agrawal, A.; Kriegel, I.; Milliron, D. J. Shape-Dependent Field Enhancement and Plasmon Resonance of Oxide Nanocrystals. *J. Phys. Chem. C* **2015**, *119* (11), 6227–6238.

(22) Buonsanti, R.; Llordes, A.; Aloni, S.; Helms, B. A.; Milliron, D. J. Tunable Infrared Absorption and Visible Transparency of Colloidal Aluminum-Doped Zinc Oxide Nanocrystals. *Nano Lett.* **2011**, *11* (11), 4706–4710.

(23) De Trizio, L.; Buonsanti, R.; Schimpf, A. M.; Llordes, A.; Gamelin, D. R.; Simonutti, R.; Milliron, D. J. Nb-Doped Colloidal TiO2 Nanocrystals with Tunable Infrared Absorption. *Chem. Mater.* **2013**, *25* (16), 3383–3390.

(24) Mattox, T. M.; Bergerud, A.; Agrawal, A.; Milliron, D. J. Influence of Shape on the Surface Plasmon Resonance of Tungsten Bronze Nanocrystals. *Chem. Mater.* **2014**, *26* (5), 1779–1784.

(25) Kim, J.; Agrawal, A.; Krieg, F.; Bergerud, A.; Milliron, D. J. The Interplay of Shape and Crystalline Anisotropies in Plasmonic Semiconductor Nanocrystals. *Nano Lett.* **2016**.

(26) Manna, G.; Bose, R.; Pradhan, N. Semiconducting and Plasmonic Copper Phosphide Platelets. *Angew. Chem. Int. Ed.* **2013**, *52* (26), 6762–6766.

(27) Comin, A.; Manna, L. New Materials for Tunable Plasmonic Colloidal Nanocrystals. *Chem. Soc. Rev.* **2014**, *43* (11), 3957–3975.

(28) Faucheaux, J. A.; Stanton, A. L. D.; Jain, P. K. Plasmon Resonances of Semiconductor Nanocrystals: Physical Principles and New Opportunities. *J. Phys. Chem. Lett.* **2014**, *5* (6), 976–985.

(29) Routzahn, A. L.; White, S. L.; Fong, L.-K.; Jain, P. K. Plasmonics with Doped Quantum Dots. *Isr. J. Chem.* **2012**, *52* (11-12), 983–991.

(30) Manthiram, K.; Alivisatos, A. P. Tunable Localized Surface Plasmon Resonances in Tungsten Oxide Nanocrystals. *J. Am. Chem. Soc.* **2012**, *134* (9), 3995–3998.

(31) Runnerstrom, E. L.; Bergerud, A.; Agrawal, A.; Johns, R. W.; Dahlman, C. J.; Singh, A.; Selbach, S. M.; Milliron, D. J. Defect Engineering in Plasmonic Metal Oxide Nanocrystals. *Nano Lett.* **2016**.

(32) Diroll, B. T.; Gordon, T. R.; Gaulding, E. A.; Klein, D. R.; Paik, T.; Yun, H. J.; Goodwin, E. D.; Damodhar, D.; Kagan, C. R.; Murray, C. B. Synthesis of N-Type Plasmonic Oxide Nanocrystals and the Optical and Electrical Characterization of Their Transparent Conducting Films. *Chem. Mater.* **2014**, *26* (15), 4579–4588.

(33) Mattox, T. M.; Ye, X.; Manthiram, K.; Schuck, P. J.; Alivisatos, A. P.; Urban, J. J. Chemical Control of Plasmons in Metal Chalcogenide and Metal Oxide Nanostructures. *Adv. Mater.* **2015**, *27* (38), 5830–5837.

(34) Gordon, T. R.; Paik, T.; Klein, D. R.; Naik, G. V.; Caglayan, H.; Boltasseva, A.; Murray, C. B. Shape-Dependent Plasmonic Response and Directed Self-Assembly in a New Semiconductor Building Block, Indium-Doped Cadmium Oxide (ICO). *Nano Lett.* **2013**, *13* (6), 2857–2863.

(35) Schimpf, A. M.; Lounis, S. D.; Runnerstrom, E. L.; Milliron, D. J.; Gamelin, D. R. Redox Chemistries and Plasmon Energies of Photodoped In2O3 and Sn-Doped In2O3 (ITO) Nanocrystals. *J. Am. Chem. Soc.* **2015**, *137* (1), 518–524.

(36) Cohn, A. W.; Janßen, N.; Mayer, J. M.; Gamelin, D. R. Photocharging ZnO Nanocrystals: Picosecond Hole Capture, Electron Accumulation, and Auger Recombination. *J. Phys. Chem. C* **2012**, *116* (38), 20633–20642.

(37) Llordes, A.; Runnerstrom, E. L.; Lounis, S. D.; Milliron, D. J. Plasmonic Electrochromism of Metal Oxide Nanocrystals. In *Electrochromic Materials and Devices*; Mortimer, R. J., Rosseinsky, D. R., Monk, P. M. S., Eds.; Wiley-VCH Verlag GmbH & Co. KGaA, 2013; pp 363–398.

(38) Faucheaux, J. A.; Jain, P. K. Plasmons in Photocharged ZnO Nanocrystals Revealing the Nature of Charge Dynamics. *J. Phys. Chem. Lett.* **2013**, *4* (18), 3024–3030.
(39) Lounis, S. D.; Runnerstrom, E. L.; Bergerud, A.; Nordlund, D.; Milliron, D. J. Influence of Dopant Distribution on the Plasmonic Properties of Indium Tin Oxide Nanocrystals. *J. Am. Chem. Soc.* **2014**, *136* (19), 7110–7116.
(40) Ghosh, S.; Saha, M.; Dev Ashok, V.; Dalal, B.; De, S. K. Tunable Surface Plasmon Resonance in Sn-Doped Zn–Cd–O Alloyed Nanocrystals. *J. Phys. Chem. C* **2015**, *119* (2), 1180–1187.
(41) Jefferson, P. H.; Hatfield, S. A.; Veal, T. D.; King, P. D. C.; McConville, C. F.; Zúñiga–Pérez, J.; Muñoz–Sanjosé, V. Bandgap and Effective Mass of Epitaxial Cadmium Oxide. *Appl. Phys. Lett.* **2008**, *92* (2), 022101.
(42) Mendelsberg, R. J.; Zhu, Y.; Anders, A. Determining the Nonparabolicity Factor of the CdO Conduction Band Using Indium Doping and the Drude Theory. *J. Phys. Appl. Phys.* **2012**, *45* (42), 425302.
(43) Kriegel, I.; Jiang, C.; Rodríguez-Fernández, J.; Schaller, R. D.; Talapin, D. V.; da Como, E.; Feldmann, J. Tuning the Excitonic and Plasmonic Properties of Copper Chalcogenide Nanocrystals. *J. Am. Chem. Soc.* **2012**, *134* (3), 1583–1590.
(44) Hartland, G. V. Optical Studies of Dynamics in Noble Metal Nanostructures. *Chem. Rev.* **2011**, *111* (6), 3858–3887.
(45) Hodak, J.; Martini, I.; Hartland, G. V. Ultrafast Study of Electron–phonon Coupling in Colloidal Gold Particles. *Chem. Phys. Lett.* **1998**, *284* (1–2), 135–141.
(46) Sun, C.-K.; Vallée, F.; Acioli, L. H.; Ippen, E. P.; Fujimoto, J. G. Femtosecond-Tunable Measurement of Electron Thermalization in Gold. *Phys. Rev. B* **1994**, *50* (20), 15337–15348.
(47) Della Valle, G.; Conforti, M.; Longhi, S.; Cerullo, G.; Brida, D. Real-Time Optical Mapping of the Dynamics of Nonthermal Electrons in Thin Gold Films. *Phys. Rev. B* **2012**, *86* (15).
(48) Soavi, G.; Tempra, I.; Pantano, M. F.; Cattoni, A.; Collin, S.; Biagioni, P.; Pugno, N. M.; Cerullo, G. Ultrasensitive Characterization of Mechanical Oscillations and Plasmon Energy Shift in Gold Nanorods. *ACS Nano* **2016**, *10* (2), 2251–2258.
(49) Hartland, G. V. Coherent Vibrational Motion in Metal Particles: Determination of the Vibrational Amplitude and Excitation Mechanism. *J. Chem. Phys.* **2002**, *116* (18), 8048–8055.
(50) Goubet, N.; Tempra, I.; Yang, J.; Soavi, G.; Polli, D.; Cerullo, G.; Pileni, M. P. Size and Nanocrystallinity Controlled Gold Nanocrystals: Synthesis, Electronic and Mechanical Properties. *Nanoscale* **2015**, *7* (7), 3237–3246.
(51) Goubet, N.; Yan, C.; Polli, D.; Portalès, H.; Arfaoui, I.; Cerullo, G.; Pileni, M.-P. Modulating Physical Properties of Isolated and Self-Assembled Nanocrystals through Change in Nanocrystallinity. *Nano Lett.* **2013**, *13* (2), 504–508.
(52) Kriegel, I.; Scotognella, F.; Soavi, G.; Brescia, R.; Rodríguez-Fernández, J.; Feldmann, J.; Lanzani, G.; Tassone, F. Delayed Electron Relaxation in CdTe Nanorods Studied by Spectral Analysis of the Ultrafast Transient Absorption. *Chem. Phys.* **2016**, *471*, 39–45.
(53) Ben-Shahar, Y.; Scotognella, F.; Waiskopf, N.; Kriegel, I.; Dal Conte, S.; Cerullo, G.; Banin, U. Effect of Surface Coating on the Photocatalytic Function of Hybrid CdS–Au Nanorods. *Small* **2015**, *11* (4), 462–471.

Insert Table of Contents artwork here